Efficient spectral coupled boundary element method for fully nonlinear wave–structure interaction simulation ⊕⊘

Shi Kaiyuan (石凯元) ⓘ ; Zhu Renchuan (朱仁传) ✉ ⓘ

Check for updates

View Online

Export Citation

CrossMark

Efficient spectral coupled boundary element method for fully nonlinear wave–structure interaction simulation ⓕ

Kaiyuan Shi (石凯元), ⓘⅅ and Renchuan Zhu (朱仁传)[a] ⓘⅅ

AFFILIATIONS

State Key Laboratory of Ocean Engineering, School of Naval Architecture, Ocean and Civil Engineering,
Shanghai Jiao Tong University, Shanghai 200240, China

Note: This paper is part of the special topic, Recent Advances in Marine Hydrodynamics.
[a]Author to whom correspondence should be addressed: renchuan@sjtu.edu.cn

ABSTRACT

Accurately analyzing wave–structure interactions is crucial for the design and operational safety of ships and marine structures. This paper presents a fully nonlinear potential-flow approach for simulating wave–structure interactions using the newly proposed spectral coupled boundary element method (SCBEM). The SCBEM efficiently models an extensive water body that encompasses structures by establishing a boundary element method (BEM) computational domain solely around the object of interest while accurately simulating the far-field broad water by a spectral layer. To further improve efficiency, graphics processing unit acceleration is hired during iterative solving of the boundary value problem in the already small-sized interior BEM domain. Simulations are conducted to validate the accuracy of the method on cases with strong nonlinear phenomena, including wave run-up on a single cylinder, diffraction of a four-cylinder array, near-trapped modes for closely spaced columns, and gap resonance that occurred in side-by-side offloading. The wave run-up, diffraction wave pattern, near-trapped mode, and gap resonance frequency obtained by the proposed method are in good agreement with data from experiments and published literature. The quite good accuracy and the exceptional computational efficiency of the SCBEM demonstrate its promising potential for more application in practical marine problems.

Published under an exclusive license by AIP Publishing. https://doi.org/10.1063/5.0151990

I. INTRODUCTION

The study of wave–structure interaction is crucial in marine engineering owing to the harsh oceanic environments that ships and floating structures endure during their lifespan. While model tests are usually considered reliable, they are time-consuming and expensive due to lengthy model fabrication and costly wave tank rental. Alternatively, thanks to the advancement of computer capabilities, numerical wave tanks (NWTs) have become popular as a cost and time-efficient alternative. Researchers can use NWT to conduct numerical experiments at any time using only a computer, eliminating the need for physical wave tanks and model fabrication.

Computational Fluid Dynamics (CFD)-based NWTs, which solve the Navier–Stokes (N–S) equations with spatial-based methods such as the finite volume method (FVM) and the finite difference method (FDM), are the most popular type of NWT.[1–3] However, accurate wave simulation with CFD-based NWTs requires an extremely dense mesh and a precise time discretization scheme to avoid numerical dissipation.[4,5] Accurate wave simulation necessitates dozens of grids along the wavelength direction and at least ten grids along the wave height direction. Moreover, similar to physical wave tanks, if the computational domain is too small, these NWTs may suffer from sidewall effects, wave reflections, and other issues.[6,7] Therefore, only a skilled user can achieve the balance between simulation efficiency and accuracy. For CFD-based NWTs, single-machine simulations typically require millions of grids and take several days.

In contrast to CFD-based NWTs, potential-based NWTs (PNWTs) neglect fluid viscosity and use Laplace's equation as the governing equation.[8–12] Ocean engineering typically involves high Reynolds numbers, which results in a flow around marine structures that can be divided into a thin boundary layer near the solid surface and an external flow beyond it.[13] This means that even with the simplification of Navier–Stokes equations to Laplace's equation, the potential-flow theory can still accurately simulate the flow fields where there is no flow separation. Given that only Laplace's equation needs

to be solved, the potential-flow theory generally offers a higher computational efficiency than CFD-based NWTs. As a result, linearized potential-flow methods have been extensively used in various engineering applications. Chen et al. proposed a semi-analytical approach that employs the null-field integral formulation with degenerate kernels to solve problems of surface-piercing porous cylinders and investigated the near-trapped mode phenomenon.[14] Fu et al. introduced a meshless generalized finite difference method (GFDM) based on linear potential-flow theory and employed GFDM to study the near-trapped mode of cylinder arrays with porous walls.[15] Gharechae and Ketabdari put forward the concept of Energy Transmission Index and examined the scattering waves and wave forces of permeable barriers and circular cylinders.[16] Wang et al. studied the hydrodynamic performance of a dual-oscillating water column device.[17] Sarkar and Chanda,[18] and Chanda et al.,[19] investigated the scattering problem of a compound porous cylinder on a porous seabed. Li and Liu conducted research on the motion of a wave energy converter under the influence of coastal reflection.[20]

However, despite being studied as early as the 1970s,[21] fully nonlinear potential-flow methods have only recently been applied to investigate the hydrodynamics of real marine structures with complex geometries.[22–25] The difficulties in implementation may lie in the treatment of instantaneous free surface and wetted body surface.

The first challenge posed by the instantaneous free surface is computational cost. Most potential-flow methods use the boundary element method (BEM) to solve Laplace's equation, which solves a dense coefficient matrix. Unlike the sparse matrices generated by spatial-based methods such as FVM, even with iterative algorithms like the generalized minimal residual method (GMRES), the computational cost for solving BEM matrix remains $O(N^2)$. Additionally, since the instantaneous free surface varies with time, BEM must construct and solve a new coefficient matrix at each time step, offsetting its advantage of using fewer grids than spatial-based methods by only discretizing the boundaries. Therefore, reducing the computational cost of solving BEM's coefficient matrix has been a major focus of researchers. Various methods have been proposed, including the use of the fast multipole method,[26–28] the Barnes–Hut algorithm,[22,25] or the pre-corrected fast Fourier transform (p-FFT) method[29–31] to decrease the time required for computing the BEM coefficient matrix product. Another effective approach is partitioning the BEM computation domain into adjacent subdomains, which transforms the dense BEM matrix into a block-diagonal matrix, which significantly reduces the computational complexity and makes it easier to solve.[32–34] Several researchers have opted not to use BEM and have instead employed other numerical methods to solve Laplace's equation. For example, Fructus and Clamond developed an iterative algorithm that processes the Dirichlet to Neumann operator.[8,9] Ducrozet et al. proposed a nonlinear wave tank without obstacles using the high-order spectral (HOS) method.[11] Engsig-Karup et al. used FDM to solve Laplace's equation and accelerated computations with graphics processing units (GPUs).[35] Shao and Faltinsen proposed a spatial-based harmonic polynomial cell (HPC) method by regarding velocity potential in each cell as a sum of basis functions.[36]

The instantaneous wetted body surface poses another challenge related to mesh discretization. During fully nonlinear potential-flow simulation, the surface mesh needs to be constantly reconstructed in order to accurately model the instantaneous wetted surface. Feng and

Bai used a structured eight-node high-order element to model the wet surface of a cylinder.[37] However, this method is only suitable for simple geometries. Another commonly adopted approach involves treating the nodes of the solid mesh as connected by virtual springs, which are compressed or extended as the waterline position changes, enabling automatic formation of a high-quality wetted surface mesh.[23,24] SHIPFLOW's MOTIONS module discretizes the entire ship mesh and refines it near the waterline. During the simulation, the mesh relative to the solid body remains fixed.[22] Harris et al. used a cubic B-spline to represent the wet surface, which shows potential for handling complex geometries.[28] However, these methods require the body surface to be transformed into a specialized mesh format prior to simulation, resulting in increased barriers to usage.

As mentioned earlier, current methods for simulating nonlinear wave–structure interactions are quite time-consuming. CFD-based NWTs typically take days to carry out simulations, while potential-based methods require several hours to accomplish a simple case. Neither of these methods can simulate exceedingly large computational domains, and considerable effort is required to prepare meshes for numerical simulation. In view of these limitations, this paper develops a novel fully nonlinear potential-flow approach for simulating wave–structure interactions. The proposed method can perform simulation within minutes, while modeling a computational domain that is tens of times larger than conventional NWTs. Moreover, it only necessitates triangular body surface meshes. By adopting the proposed spectral coupled boundary element method (SCBEM), the entire computational domain is partitioned into a small BEM domain that tightly encloses the object of interest and a broad spectral layer outside the BEM domain. The near-field flow in the BEM domain is described using unstructured scattered points. The wetted surface mesh is then determined by directly cutting the complete surface mesh with the water surface. To further improve efficiency, the GMRES method is employed to solve the BEM domain equation, and GPU is utilized to accelerate the computation of the matrix–vector product in GMRES.

For validation, wave run-up on a single cylinder, diffraction of a four-cylinder array, and the near-trapped modes are simulated. The results are compared with experimental data and other numerical methods in published literature. The proposed method achieves simulation accuracy comparable to CFD-based NWTs while being significantly faster. Furthermore, long-term white-noise spectrum simulations of gap resonance due to side-by-side offloading are performed. Results verify the proposed method in simulating irregular wave responses. For such a scenario where viscous effects are significant, the proposed method can provide flow field characteristics under an inviscid perspective for comparison with experimental or viscous CFD simulations to gain further insight into the role of viscosity in the underlying physics.

II. MATHEMATICAL MODEL AND NUMERICAL IMPLEMENTATION

A. Mathematical model

1. Governing equations in the open sea

Assuming that the fluid is homogeneous, incompressible, and inviscid, the flow is irrotational, and using a Cartesian coordinate system established with the z-axis oriented vertically upward and the origin located at the calm water surface, according to the potential-flow

theory, there exists a velocity potential function ϕ that satisfies Laplace's equation; the velocity in the flow field is equal to the gradient of the velocity potential function ϕ,

$$\nabla^2 \phi(\boldsymbol{x}, z) = 0, \quad (1)$$

$$(u, v, w) = \nabla\phi, \quad (2)$$

where ∇^2 represents the Laplace operator, $\boldsymbol{x} \equiv (x, y)$ denotes the horizontal coordinates, and (u, v, w) are the velocities in three dimensions of the flow field.

The free surface must satisfy the following kinematic and dynamic conditions:

$$\frac{\partial \zeta}{\partial t} = \frac{\partial \phi}{\partial z} - \nabla_x \phi \cdot \nabla_x \zeta \qquad \text{on} \quad S_f, \quad (3)$$
$$\frac{\partial \phi}{\partial t} = -g\zeta - \frac{(\nabla\phi)^2}{2}$$

where S_f represents the instantaneous free surface, ζ denotes the wave elevation, g is the gravitational acceleration, and $\nabla_x \equiv (\partial/\partial x, \partial/\partial y)$ stands for the spatial derivative in the horizontal direction.

The dynamic nature of the free surface, which continuously changes over time, poses challenges for numerical simulations. To address this issue, Zakharov proposed treating the velocity potential on the free surface as a single-valued function in the horizontal direction and introduced the surface potential $\phi^S(\boldsymbol{x}) = \phi(\boldsymbol{x}, \zeta(\boldsymbol{x}))$. Then, the free surface condition can be expressed as:[38]

$$\frac{\partial \zeta}{\partial t} = \left(1 + (\nabla_x \zeta)^2\right) \frac{\partial \phi}{\partial z} - \nabla_x \phi^S \cdot \nabla_x \zeta$$
$$\frac{\partial \phi^S}{\partial t} = \frac{1 + (\nabla_x \zeta)^2}{2} \left(\frac{\partial \phi}{\partial z}\right)^2 - g\zeta - \frac{(\nabla_x \phi^S)^2}{2} \qquad \text{on} \quad S_f. \quad (4)$$

In addition, the flow field must satisfy the no-penetration condition at the body surface S_b, written as

$$\frac{\partial \phi}{\partial n} = (\boldsymbol{U} + \boldsymbol{\Omega} \times \boldsymbol{r}) \cdot \boldsymbol{n} \quad \text{on} \quad S_b, \quad (5)$$

where $\boldsymbol{n}$ is the normal vector to the solid surface and $\partial/\partial n$ denotes the derivative in the direction normal to the surface. $\boldsymbol{U}$ and $\boldsymbol{\Omega}$ represent the translational and angular velocities of the body, respectively.

Finally, the flow must satisfy the bottom boundary condition of infinite depth, written as

$$\frac{\partial \phi}{\partial z} = 0 \quad \text{as} \quad z \to -\infty. \quad (6)$$

2. Wave generation and absorption

Assume a large computational domain with a marine structure located at the center, where incident waves interact with the structure and generate scattered waves. The total velocity potential in the computational domain can be denoted as ϕ_{total}, and the incident velocity potential without any structures presents as $\phi_{incident}$. The scattered velocity potential $\phi_{scatter}$ induced by the incident waves can then be calculated by subtracting $\phi_{incident}$ from ϕ_{total},

$$\phi_{scatter} = \phi_{total} - \phi_{incident}. \quad (7)$$

Scattered waves generated by the structure propagate outward to infinity. However, when simulating an unbounded ocean environment

using a finite computational domain, it is necessary to prevent unrealistic wave reflections at the domain boundaries that can interfere with accurate calculations. We introduce an artificial dissipation term in the dynamic condition given by Eq. (4) to absorb scattered waves near the domain boundary,

$$\frac{\partial \phi^S}{\partial t} = \frac{1 + (\nabla_x \zeta)^2}{2} \left(\frac{\partial \phi}{\partial z}\right)^2 - g\zeta - \frac{(\nabla_x \phi^S)^2}{2} - \mu\phi_{absorb}^S. \quad (8)$$

Here, $\phi_{absorb}^S = \phi_{scatter}(\boldsymbol{x}, \zeta(\boldsymbol{x}))$ represents the velocity potential to be absorbed on the free surface. μ is an artificial dissipation function that dissipates wave kinetic energy. The regions where μ takes non-zero values are referred to as a damping zone, which are arranged at the inner margin of the computational domain. To guarantee adequate damping, the width of the damping zone must exceed the characteristic wavelength.[39] In this study, the width of the damping zone for scattered waves is one-fourth of the total length of the computational domain, gradually increasing from 0 to 0.05.

To obtain the incident potential that satisfies the nonlinear free surface conditions, we perform a separate numerical simulation without the structure and refer to it as the incident wave domain. The size of this domain is the same as that of the computational domain containing the marine structure. To generate the target incident waves, we set up a wave-making zone upstream in the incident wave domain,

$$\zeta_{incident} = (1 - R(x))\zeta_{incident} + R(x)\zeta_{target},$$
$$\phi_{incident}^S = (1 - R(x))\phi_{incident}^S + R(x)\phi_{target}^S. \quad (9)$$

In Eq. (9), ζ_{target} and ϕ_{target}^S are the artificially defined target wave functions, which can be obtained using theoretical formulas such as the fifth-order Stokes wave for generating regular waves.[40] The ramping function $R(x)$ is non-zero only within the wave-making zone and zero elsewhere. A wave-damping zone downstream is also arranged based on Eq. (8). For the incident wave domain, $\phi_{absorb}^S = \phi_{target}(\boldsymbol{x}, \zeta(\boldsymbol{x}))$. Figure 1 shows the wave-making ramping function and artificial damping function used in the incident wave domain, where L_x represents the total length of the domain along the x-axis. The incident waves are generated in the wave-making zone and propagate forward until they dissipate in the wave-damping zone. Since the waves at both ends of the domain are zero, the incident velocity potential designed in this way also satisfies periodic boundary conditions.

B. Spectral coupled boundary element method

1. Discretization of the computational domain

To solve the boundary conditions described in Sec. II A, we adopt a combination of a background mesh and local node refinement to
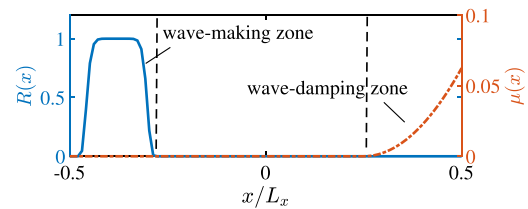

FIG. 1. Wave-making ramp function and artificial damping function for the incident wave computational domain.
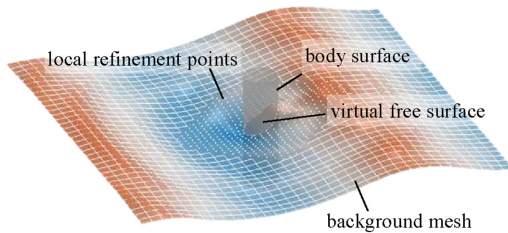
FIG. 2. Numerical discretization of the free surface.

discretize the free surface, as illustrated in Fig. 2. The background mesh provides a coarse grid for the entire computational domain, while the local node refinement technique involves the refined collocation points in areas where the flow field undergoes significant changes near the structure. This approach enables higher mesh resolution to be achieved where it is needed while minimizing computational costs in areas far from the structure where the waves are relatively mild. Figure 2 also depicts a *virtual free surface* inside the solid body, even though there is no actual free surface, and no collocation points are used for numerical discretization. The virtual free surface is obtained by applying radial basis function (RBF) interpolation to refined scattered points and plays an important role in the SCBEM.

As shown in Fig. 3, a triangular mesh is employed to discretize the initial complete solid surface. Once the virtual free surface is known, it can be used to readily cut the complete solid surface and generate the instantaneous wet surface mesh. The triangular mesh is supported by almost all mesh generation software and can represent any geometry, making it widely applicable. However, this approach also leads to increased discretization quantities and inconsistencies in the number of wet surface meshes involved in the computation at each time step. Therefore, it is necessary to apply an appropriate solution method, which will be discussed later in this paper.

If the surface potential ϕ^S and wave elevation ζ are known at a certain time for both the background mesh and locally refined points, along with the body's velocity (which is zero in the cases discussed in this paper), Eq. (4) can be solved to obtain the time derivative of ϕ^S and ζ. The temporal integration is performed using the fourth-order Runge–Kutta method. Equation (4) involves known quantities $\zeta(\boldsymbol{x})$ and $\phi^S(\boldsymbol{x})$, whose horizontal derivatives can be easily computed using numerical methods like finite difference. The only variable that cannot be directly calculated is the vertical velocity on the free surface, $\partial\phi/\partial z$. To obtain this value, the following Dirichlet–Neumann boundary value problem (BVP) must be solved at each time step,
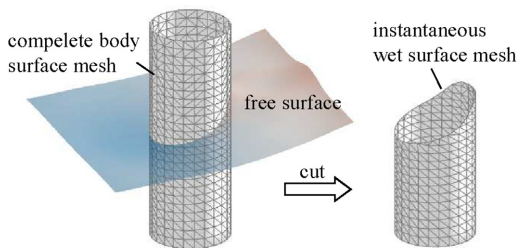

FIG. 3. Discretization of the initial complete solid surface and the instantaneous wet surface.

$$\begin{cases} \phi(\boldsymbol{x}, z) = \phi^S & \text{on } S_f, \\ \dfrac{\partial\phi(\boldsymbol{x}, z)}{\partial n} = (\boldsymbol{U} + \boldsymbol{\Omega} \times \boldsymbol{r}) \cdot \boldsymbol{n} & \text{on } S_b, \\ \dfrac{\partial\phi}{\partial z} = 0 & \text{as } z \to -\infty. \end{cases} \quad (10)$$

2. Domain decomposition strategy

Solving the BVP in Eq. (10) is the most time-consuming part of the fully nonlinear potential-flow approach. As previously stated, using only BEM leads to a sharp increase in computation time with $O(N^2)$ complexity as the discretization quantity rises. This limitation often confines fully nonlinear potential-flow simulations to small calculation domains. To simulate a larger calculation domain with minimal computational cost, this paper utilizes a domain decomposition strategy. By exploiting the linearity property of Laplace's equation, the SCBEM divides the original BVP in Eq. (10) into two parts: a spectral part and a BEM part. The BVP for the spectral layer is given by

$$\begin{cases} \phi^H = T\phi^S & \text{on } S_{f*}, \\ \dfrac{\partial\phi^H}{\partial z} = 0 & \text{as } z \to -\infty. \end{cases} \quad (11)$$

where ϕ^H denotes the velocity potential for the spectral layer, S_{f*} is the virtual free surface, and T is the transition function.

The remaining BVP is solved by BEM as follows:

$$\begin{cases} \phi^R = (1 - T)\phi^S & \text{on } S_f, \\ \dfrac{\partial\phi^R}{\partial n} = -\dfrac{\partial\phi^H}{\partial n} + (\boldsymbol{U} + \boldsymbol{\Omega} \times \boldsymbol{r}) \cdot \boldsymbol{n} & \text{on } S_b, \\ \dfrac{\partial\phi^R}{\partial z} = 0 & \text{as } z \to -\infty, \end{cases} \quad (12)$$

where ϕ^R denotes the velocity potential for the BEM domain.

The total vertical velocity of the computational domain on the free surface is obtained by adding the contributions from the spectral layer and the BEM domain,

$$\frac{\partial\phi(\boldsymbol{x}, \zeta)}{\partial z} = \frac{\partial\phi^H(\boldsymbol{x}, \zeta)}{\partial z} + \frac{\partial\phi^R(\boldsymbol{x}, \zeta)}{\partial z}. \quad (13)$$

Although the number of BVPs to be solved has increased from one to two, the use of a transition function T can significantly reduce the difficulty of solving the problem. As shown in Fig. 4, the transition function is a smooth function that is 0 near the body surface and 1 at far-field. By dividing the original BVP into a spectral part and a BEM part using the transition function, the near-field Dirichlet condition for the spectral layer is 0, and the far-field Dirichlet condition for the BEM domain is also 0. We define the region where T is not equal to 1 as the BEM domain, with the area where $T = 0$ as the inner BEM zone, and the area with $0 < T < 1$ as the transition zone. The expression for T is given by

$$T = \begin{cases} 0 & \text{in the inner BEM zone,} \\ 1 - T_x T_y & \text{in the transition zone,} \\ 1 & \text{outside the BEM domain,} \end{cases} \quad (14)$$
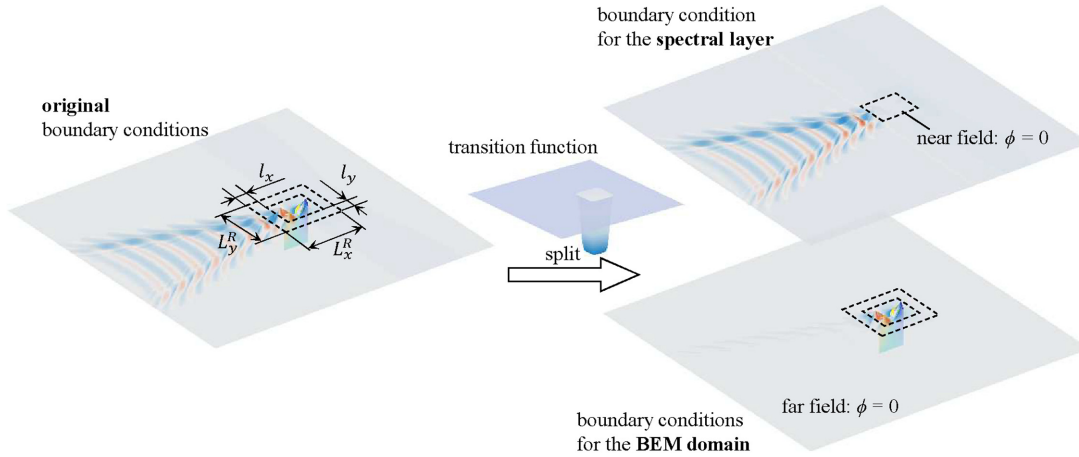
where

FIG. 4. Domain decomposition of the boundary value problem (colors indicate the boundary value).

$$T_x = \frac{1}{2}\left(\mathrm{erf}\left(2 - \frac{4d_x}{l_x}\right) + 1\right),$$
$$T_y = \frac{1}{2}\left(\mathrm{erf}\left(2 - \frac{4d_y}{l_y}\right) + 1\right). \tag{15}$$

As shown in Fig. 4, the BEM domain is a rectangular area with length L_x^R and width L_y^R. In Eq. (15), l_x and l_y are the widths of the transition zone, while d_x and d_y are the distances from any point within the BEM domain to the nearest boundary along x-axis and y-axis, respectively. Generally, a wider transition zone can achieve better coupling effects. Shi *et al.* used SCBEM to simulate various types of nonlinear waves, and the results show that when the width of the transition zone is greater than half the wavelength of the simulated wave, the accuracy of the wave simulation can be ensured.[41]

To solve the BVP in the spectral layer, we start by interpolating the virtual free surface ζ and velocity potential ϕ^S into an equidistant mesh. Then, we use the high-order spectral (HOS) method to efficiently compute the vertical velocity on the virtual free surface with a time complexity of $O(N \log N)$. Due to space limitations, this paper only presents the relevant calculation formulas, and more details on numerical implementation can be found in Refs. 42 and 43.

As a pseudo-spectral method, the HOS method views the total velocity potential as a superposition of modal functions that satisfy the Laplace's equation and infinite depth condition,

$$\phi^H(\mathbf{x}, z) = \mathrm{Re}\left(\sum_j A_j \exp\left(|\mathbf{k}_j| z + i\mathbf{k}_j \cdot \mathbf{x}\right)\right), \tag{16}$$

where $\mathbf{k} \equiv (k_x, k_y)$ denotes the wavenumber vector and A_j represents the amplitude of the velocity potential component corresponding to $\mathbf{k}_j$.

Through the use of perturbation and Taylor expansions, the total velocity potential ϕ^H can be decomposed into a series of velocity potentials $\phi^{(i)}$ at various orders. The values of each order's velocity potential at the $z = 0$ are then calculated using the following equations:

$$\phi^{(1)}(\mathbf{x}, 0) = \phi^S,$$
$$\phi^{(m)}(\mathbf{x}, 0) = -\sum_{k=1}^{m-1} \frac{\zeta^k}{k!} \frac{\partial^k}{\partial z^k}\left(\phi^{(m-k)}(\mathbf{x}, 0)\right), \quad m > 1. \tag{17}$$

Since an equidistant grid is used for discretization, the amplitude of each modal function can be efficiently obtained using the fast Fourier transform (FFT) once their values at $z = 0$ are known. The vertical velocity of the free surface $\partial \phi^H / \partial z$ can then be calculated by

$$\frac{\partial \phi^H(\mathbf{x}, \zeta)}{\partial z} = \sum_{k=1}^{M}\left(\frac{\zeta^{k-1}}{(k-1)!} \frac{\partial^k}{\partial z^k} \sum_{m=1}^{M-k+1} \phi^{(m)}(\mathbf{x}, 0)\right), \tag{18}$$

where M denotes the truncation order. Since the spectral layer in the SCBEM is only used to model the far-field velocity potential and does not have a significant wave slope, we set $M = 3$ in this paper.

C. BEM equation solution with GPU acceleration

1. Desingularized Rankine panel method

Building on the SCBEM given in Sec. II B, the far-field Dirichlet condition for the BEM domain is simplified to zero. In this paper, we solve the BVP in the BEM domain within the framework of the desingularized Rankine panel (DRP) method,[44] which is an indirect boundary element method (also known as the method of fundamental solutions). The DRP method involves placing constant panels on the body surface and desingularized point sources above the free surface collocation points. Both panel source and point source satisfy Laplace's equation and the infinite depth boundary condition.

The velocity potential induced by the desingularized point source i located at $\boldsymbol{\xi}_i(\xi, \eta, \zeta)$ is written as

$$G_i^{pt}(x, y, z) = \frac{1}{\sqrt{(x-\xi)^2 + (y-\eta)^2 + (z-\zeta)^2}}. \tag{19}$$

The velocity potential induced by the constant panel element located on S_i is written as

$$G_i^{pan}(x, y, z) = \iint_{S_i} \frac{1}{\sqrt{(x-\xi)^2 + (y-\eta)^2 + (z-\zeta)^2}} dS. \tag{20}$$

The source strength distribution satisfies the Dirichlet condition on the free surface collocation points,

$$\sum_{i=1}^{N_{pt}} \sigma_i^{pt} G_i^{pt}(x_j, y_j, z_j) + \sum_{i=1}^{N_{pan}} \sigma_i^{pan} G_i^{pan}(x_j, y_j, z_j)$$
$$= \phi^R(x_j, y_j, z_j) \quad (x_j, y_j, z_j) \in S_f, \tag{21}$$

and the Neumann condition at the center of the panel elements

$$\sum_{i=1}^{N_{pt}} \sigma_i^{pt} \frac{\partial}{\partial n_j} G_i^{pt}(x_j, y_j, z_j) + \sum_{i=1}^{N_{pan}} \sigma_i^{pan} \frac{\partial}{\partial n_j} G_i^{pan}(x_j, y_j, z_j)$$
$$= \frac{\partial}{\partial n_j} \phi^R(x_j, y_j, z_j) \quad (x_j, y_j, z_j) \in S_b, \tag{22}$$

where N_{pt} and N_{pan} denote the number of point sources and panel elements, respectively, while σ_i^{pt} and σ_i^{pan} represent the unknown source strengths. Dirichlet conditions must be satisfied on the N_{pt} collocation points located below the point sources, and Neumann conditions must be satisfied at the N_{pan} locations corresponding to the center of each panel element. Thus, the equations are closed. Once the source strength distribution is obtained, the vertical velocity of the free surface can be calculated using the following equation:

$$\frac{\partial \phi^R}{\partial z} = \sum_{i=1}^{N_{pt}} \sigma_i^{pt} \frac{\partial}{\partial z} G_i^{pt} + \sum_{i=1}^{N_{pan}} \sigma_i^{pan} \frac{\partial}{\partial z} G_i^{pan}. \tag{23}$$

In numerical implementation, sources are selectively placed only in the rectangular BEM domain where the transition function is $T \neq 1$ for the SCBEM. The decay in velocity potential induced by the sources in the DRP method at increasing distances leads us to assume that the far-field Dirichlet condition $\phi^R(x, \zeta(x)) = 0$ is automatically satisfied outside the BEM domain. Consequently, regardless of the size of the total computational domain, the SCBEM requires only a small BEM domain established surrounding the body surface, resulting in significant savings of computational resources.

2. Lyness quadrature rule

In the DRP method, the desingularized point sources are placed above the collocation points, which eliminates the need to deal with singularity when evaluating the velocity potential on the free surface. However, when calculating the velocity potential induced by the body surface, the field point may lie on the panel element, resulting in a weak singularity in the integral. To ensure accuracy, this study employs the analytical integration method proposed by Hess and Smith[45] to evaluate the induced velocity potential when the source panel is close to the field point. However, when the source panel is far from the field point, the Lyness three-point quadrature rule[46] can be adopted to simplify the calculation of the velocity potential, written as

$$G^{pan}(P) \approx \frac{A}{3} \left(\frac{1}{||PQ_1||_2} + \frac{1}{||PQ_2||_2} + \frac{1}{||PQ_3||_2} \right), \tag{24}$$

where $P = (x, y, z)$ is the field point located far from the source panel, A denotes the area of the source panel, and Q_1, Q_2, and Q_3 represent the midpoints of the three sides of the triangular source panel. The Euclidean distance between two points is denoted by $||PQ_i||_2$.

3. Computation of source strength distribution

At each time step, the BEM domain requires solving the equation $Ax = b$ to find a suitable source strength distribution x that satisfies the boundary conditions. However, direct matrix solution incurs computational costs on the order of $O(N^3)$, rendering it impractical. In this study, the GMRES method is employed to iteratively solve the equation, achieving desired accuracy after tens to hundreds of iterations. The primary computational expense during the iterative process arises from the repeated calculation of the product Ax between the coefficient matrix and the source distribution vector. Thus, this section focuses on investigating fast methods to compute Ax.

As previously discussed, the Lyness quadrature rule can approximate the velocity potential induced by the source panel when it is far from the field point. Moreover, if the Lyness quadrature rule is used when the source panel is close to the field point, the panel can be completely replaced with its three side midpoints. This approach results in a linear operator denoted as A^{Lyn}, and the coefficient matrix can be decomposed as follows:

$$Ax = A^{Lyn}x + A^{Patch}x. \tag{25}$$

Here, A^{Patch} denotes the sparse patch matrix. If the distance between the source panel and the field point is large, the Lyness quadrature can provide accurate results without requiring any correction. Therefore, A^{Patch} is only non-zero when the source panel is close to the field point. Due to its sparsity, the computational cost of $A^{Patch}x$ is $O(N)$, which is insignificant compared to that of $A^{Lyn}x$.

The Lyness term $A^{Lyn}x$ represents the impact of a series of point sources on field points. Such computations are common in N-body simulations, and their direct calculation has a time complexity of $O(N^2)$. However, this complexity can be reduced to $O(N)$ by using the fast multiple method (FMM) or other tree algorithms. To determine the most suitable computational approach, N source points and N field points are generated randomly, and FMM and direct methods are employed to compute the velocity potential and velocity at all field points. The process is repeated multiple times to obtain the averaged computation time. All calculations in this paper are performed on a PC with an AMD 3700X CPU, Nvidia RTX2060 GPU, and 16 GB memory, using single-precision floating-point numbers. The FMM program used for comparison employs the miniFMM open-source code,[47] while the program for direct methods is developed in-house and implemented on the OpenCL platform for GPU acceleration.

Figure 5 shows the computation time for different methods applied to compute interactions. The direct methods exhibit three curves with a slope of approximately 2 when the number of nodes N is large, while the FMM exhibits three curves with a slope of approximately 1. These slopes are consistent with the theoretical time complexities of $O(N^2)$ and $O(N)$ for the two methods, respectively. Remarkably, for $N \approx 10^4$, the direct method on GPU displays significantly superior efficiency compared to other computational approaches, with a computation time of only approximately 1.5 ms. With the implementation of SCBEM, the BEM domain only needs to be arranged near the structure, resulting in a number of unknowns on the order of 10^4. This makes the GPU-accelerated direct method the optimal choice in terms of computational performance. Consequently, we select the GPU-based direct method as the kernel for computing $A^{Lyn}x$, achieving the highest computational efficiency.
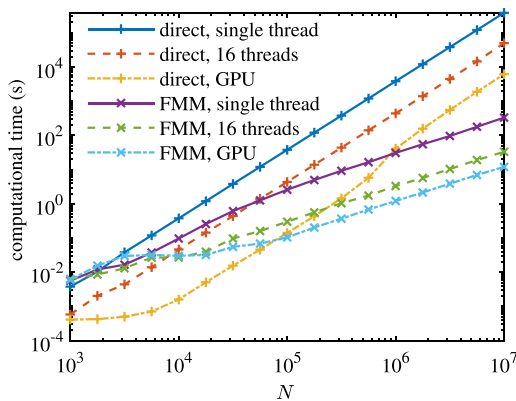
FIG. 5. Time consumption for different methods.

Figure 6 illustrates the process of SCBEM for each sub-time step during the integration of flow field using the Runge–Kutta method. Initially, given the free surface elevation ζ and free surface potential ϕ^S, the holes caused by the presence of solid surfaces are patched to obtain the virtual free surface ζ^*. Subsequently, the instantaneous wetted surface mesh is generated by cutting the complete surface mesh. The BVP $\phi^H(x, \zeta^*) = T\phi^S$ is solved by means of the HOS method, and the HOS contribution is subtracted from the original BVP to obtain the BVP in Eq. (12), which is then solved iteratively using the BEM presented in this section. Finally, combining the contributions of both the HOS part and the BEM part provides the total vertical
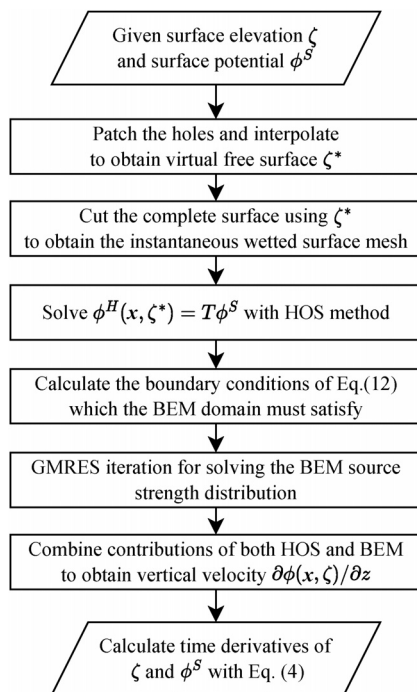
velocity of the free surface, i.e., $\partial\phi(x, \zeta)/\partial z$, which is substituted into Eq. (4) to determine the temporal derivatives of ζ and ϕ^S.

D. Other numerical implementations

1. Radial basis function interpolation

The free surface near the solid surface is discretized as scattered points, without any structured background grid. As a result, it is challenging to compute horizontal derivatives and perform interpolation. To address this issue, we utilize the RBF method to construct a surface from these scattered points, enabling more efficient and accurate calculations of interpolation and derivative values. As shown in Fig. 7, for scattered points on the near-field free surface, we first search for nearby points within a radius of 3.5 grid lengths. We then use thin plate spline (TPS) as the radial basis function to construct a linear equation system and obtain interpolation coefficients. The resulting surface is constructed based on these thin plate spline functions and can be expressed as

$$f(x) = \sum_{i=1}^{n} c_i \varphi(||x - x_i||_2), \qquad (26)$$

where x_i is the center location of the TPS basis, operator $|| \ ||_2$ denotes the ℓ^2 norm of the vector, and $\varphi(r)$ is the TPS function, defined as $\varphi(r) = r^2 \log r$. The interpolation coefficients c_i are obtained by solving the following equation system:

$$\begin{bmatrix} \varphi(r_{11}) + s & \cdots & \varphi(r_{1n}) \\ \vdots & & \vdots \\ \varphi(r_{n1}) & \cdots & \varphi(r_{nn}) + s \end{bmatrix} \begin{bmatrix} c_1 \\ \vdots \\ c_n \end{bmatrix} = \begin{bmatrix} f(x_1) \\ \vdots \\ f(x_n) \end{bmatrix}. \qquad (27)$$

Here, $r_{ij} = ||x_i - x_j||_2$ and s is the smoothing factor added to the diagonal of the RBF matrix. The inclusion of the smoothing factor can reduce the condition number of the matrix and also result in a smoother surface. Furthermore, it can filter out high-frequency wave components to suppress the *sawtooth instability* in time-domain simulations. Due to the adoption of RBF, it is not necessary to maintain consistent discretization schemes for the computational domain at each time step. After each time step, RBF interpolations are performed to obtain the wave height ζ and velocity potential ϕ^S at the newly discretized points for the next time step.

2. Pre-breaking wave treatment

During the simulation of highly nonlinear conditions, wave overturning and breaking may occur. To ensure the stability of the
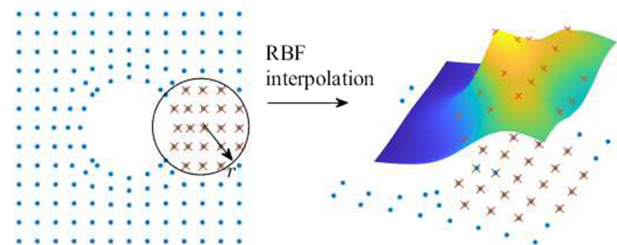

FIG. 6. Flowchart for computing temporal derivatives of the flow field using SCBEM.

FIG. 7. Basis search and surface reconstruction with the Radial Basis Function method.
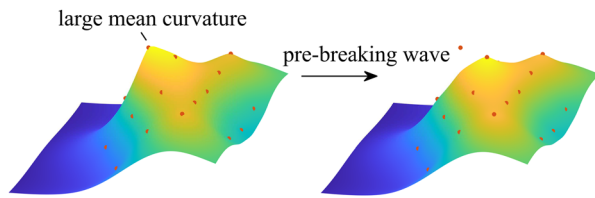
FIG. 8. Detection and reconstruction of wave breaking points.

potential-flow simulation and prevent any collapse due to wave break-ing, a pre-breaking wave treatment is introduced into the simulation process. This treatment is designed to detect steep waves with the potential for breaking and thereby reduce their kinetic and potential energy in advance, thus preventing any future wave breaking.

After constructing the RBF surface for the discretized points on the free surface, we calculate the mean curvature of each point as shown in Fig. 8. If the mean curvature exceeds a certain threshold ε, it indicates that the wave is excessively steep at that location and may experience wave-breaking. In this case, we exclude the breaking point and reconstruct the RBF surface. We then perform an interpolation to obtain the wave height and velocity potential values at the breaking position, which are used as the corrected flow field information in sub-sequent time-domain simulation.

In this study, we set the breaking threshold to $\varepsilon = 1.8$. It is important to note that this pre-breaking wave treatment is only a numerical trick to ensure the stability of the potential-flow simulation and does not simulate real breaking waves. This limitation is one of the drawbacks of the method. In the future, more physically realistic three-dimensional wave-breaking models can be applied to improve the wave-breaking treatment.

III. NUMERICAL VALIDATION

A. Wave run-up on a single cylinder

1. Numerical setup

To validate the accuracy of our fully nonlinear PNWT, this sec-tion performs numerical simulations that reproduce the benchmark experiment organized by the Ocean Engineering Committee at the 27th International Towing Tank Conference (ITTC).[48] The numerical results are compared against experimental data and published litera-ture. The experiment involves a cylindrical column with a radius of 8 m and a depth of 24 m in prototype scale, conducted at MOERI wave tank in South Korea. Several wave probes are arranged around the cylinder to measure wave height, as shown in Fig. 9. Probes WPB1–WPB5 are uniformly spaced at 45° intervals near the cylinder wall, with a distance of 8.2063 m from the cylinder center. Probes WPO1–WPO5 are uniformly distributed on the outer side, at a dis-tance of 16 m from the center. For the numerical simulations pre-sented in this subsection, regular waves with a wave period $T = 9$ s are generated as an incident wave, and the wave parameters for each sce-nario are presented in Table I.

The computational domain parameters for the SCBEM are pre-sented in Table II. The numerical simulations utilize a background mesh spacing of 5 m and 250 000 background nodes, constructed into a large computational domain size of 2560×2560 m^2, which is 20 times the wavelength of the incident wave. A BEM domain with a size
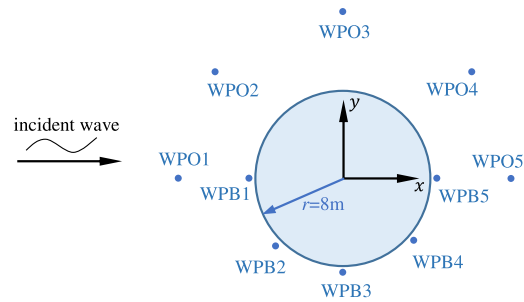

FIG. 9. Probes layout for wave run-up experiments on a single cylinder (in proto-type scale).

TABLE I. Incident wave parameters for wave run-up experiments on a single cylin-der (in prototype scale).

Name	Period T (s)	Steepness H/L	Height H (m)
T09S130	9	1/30	4.262
T09S116	9	1/16	8.215

TABLE II. Parameters of the computational domain for SCBEM simulation of wave run-up on a single cylinder.

Parameter	Value
Background mesh spacing	5 m
Transition zone width	120 m
Size of the entire computational domain	2560×2560 m^2
Size of the BEM domain	400×400 m^2
Size of the inner BEM zone	160×160 m^2

of 400×400 m^2 is centered on the background mesh, which is only three times the wavelength of the incident wave. To ensure adequate coupling between the BEM domain and the spectral layer, a transition zone with a width of 120 m, roughly comparable to the wavelength of the incident wave, is included. Figure 10 shows an overview of the computational domain used in the PNWT, demonstrating that our approach can simulate a fairly wide free surface area, closer to the physical reality of an unbounded ocean.

2. Convergence analysis

To ensure that the simulation results of the fully nonlinear PNWT are not influenced by simulation parameters, such as time step and mesh resolution, convergence analysis is conducted. Three sets of meshes with different resolutions are established, with varying num-bers of panel elements and locally refined nodes, as presented in Table III. The distribution of nodes near the water surface and the cylinder surface panel elements for the three grids are illustrated in Figs. 11 and 12, respectively.

Timestep convergence analysis is first conducted on mesh B using the T09S130 incident wave with a period of $T = 9$ s and wave steepness of $H/L = 1/30$. Numerical simulations are performed with
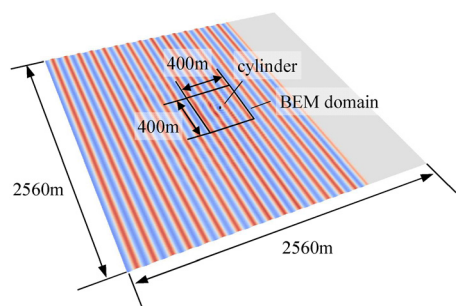
FIG. 10. Overview of the computational domain.

TABLE III. Mesh parameters for the convergence analysis.

Name	Panel number	Refined node spacing	Refined node number
Mesh A	528	4.5 m	168
Mesh B	1272	3.0 m	396
Mesh C	2436	2.0 m	952

time steps of $\Delta t = 0.05, 0.1$, and 0.2 s. The wave elevation time history at probes WPB1 and WPO5 is shown in Fig. 13. The wave elevations at these two probes for the three different time steps are nearly identical, irrespective of whether the measurement point is near the cylinder (WPB1) or downstream (WPO5). These results indicate that the present method converges with sufficiently small time steps.
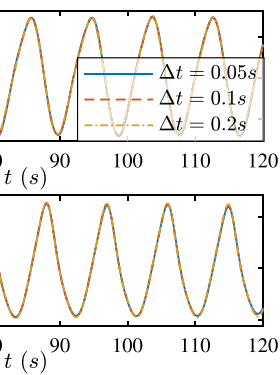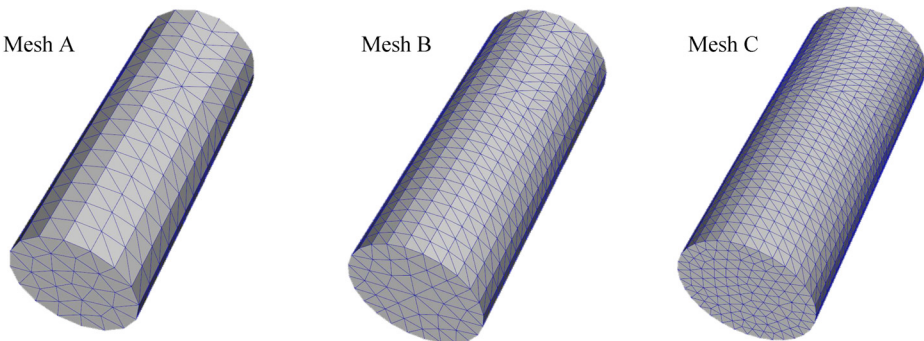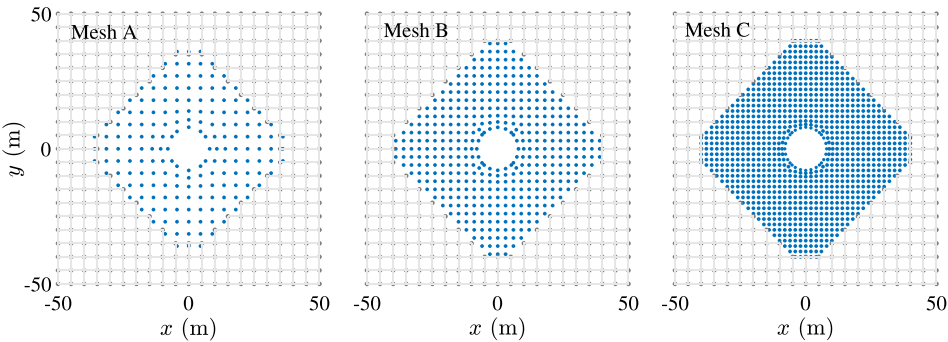

FIG. 13. Time history of wave elevation with different timesteps. (a) WPB1 and (b) WPO5.

Wave run-up simulations are performed for meshes A, B, and C with sufficiently small time steps under the T09S130 incident wave, as shown in Fig. 14. The wave elevations at probes for meshes B and C are nearly identical, whereas some minor differences can be observed at WPB1 for mesh A, which may be attributed to its relatively low mesh density. The convergence analysis confirms that the present method converges with increasing mesh resolution. Considering the accuracy provided by mesh B, we will employ it for subsequent numerical simulations.

Table IV shows the simulation timesteps and average wall time per wave period for meshes A, B, and C under T09S130. The results illustrate that our method is highly computationally efficient. The total

FIG. 11. Distributions of nodes near the waterline.
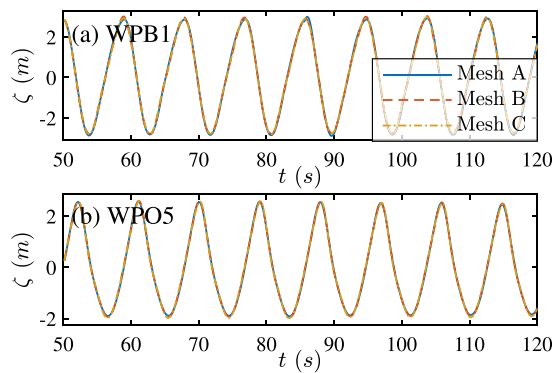

FIG. 12. Panel elements for different meshes.

FIG. 14. Time history of wave elevation with different meshes. (a) WPB1 and (b) WPO5.

TABLE IV. Time consumption with different meshes for the simulation of wave run-up.

Name	Timestep (s)	Time consumption per period (s)
Mesh A	0.20	18.5
Mesh B	0.20	19.2
Mesh C	0.15	35.1

number of nodes used in our simulations is 260 000, which is much higher than the typical number of unknowns employed in other PNWTs. If only the BEM method were employed, the computation time would be prohibitively long. However, we reduce the BEM computation domain to near the cylinder surface using the SCBEM, resulting in only approximately 10 000 discretized unknowns for the BEM domain. The GMRES solver along with GPU-accelerated matrix

product calculation effectively exploits the advantages of GPU computing, enabling simulation times of just a few tens of seconds per wave period. Compared to CFD-based NWTs that take several hours per wave period for simulation, the proposed PNWT utilizing SCBEM demonstrates impressive efficiency advantages.

3. Analysis of numerical results

Figure 15 compares the wave elevation time histories at different probes under the T09S116 scenario obtained using various methods. The figure presents simulation results from our SCBEM simulation, experimental data from the MOERI wave tank,[48] numerical results from Sun *et al.* using OpenFOAM, and results from the DIFFRACT program based on the frequency domain second-order potential-flow theory.[49] In the OpenFOAM simulation, a laminar model is used to solve the N–S equations. The results show that, except for WPB4, SCBEM results are in good agreement with the experimental and OpenFOAM results and outperform the predictions from DIFFRACT. Specifically, DIFFRACT significantly underestimates the wave trough values at WPB3 and WPB4, whereas our method and OpenFOAM accurately predict these wave troughs, demonstrating that our PNWT more accurately accounts for the effects of high-order nonlinearity than DIFFRACT.

Figure 16 draws the wave pattern before and after a wave crest passes through the cylinder. The figure clearly illustrates the Type-1 scattered waves radiating outward from the cylinder center and the Type-2 scattered waves that are symmetrically distributed along the incident direction but do not have the cylinder as the center, consistent with the experimental findings of Swan and Sheikh.[50] These scattered waves are often characterized by high steepness and strong nonlinearity. During the time of Figs. 16(b) and 16(d), the proposed PWNT detected extremely high local steepness exceeding the breaking limit and triggered the pre-breaking treatment. The wave height and velocity potential at the breaking position were significantly reduced after
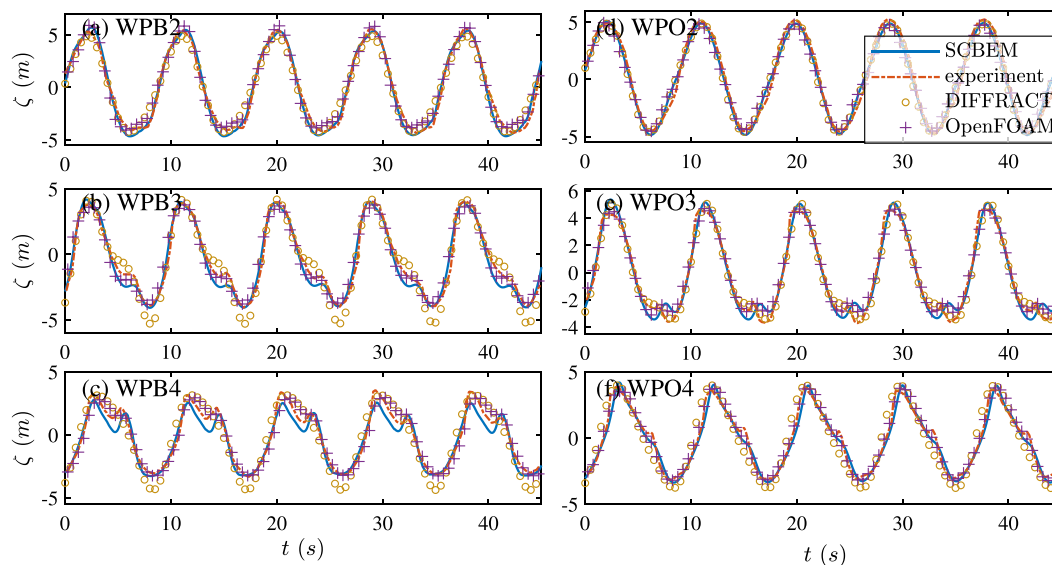

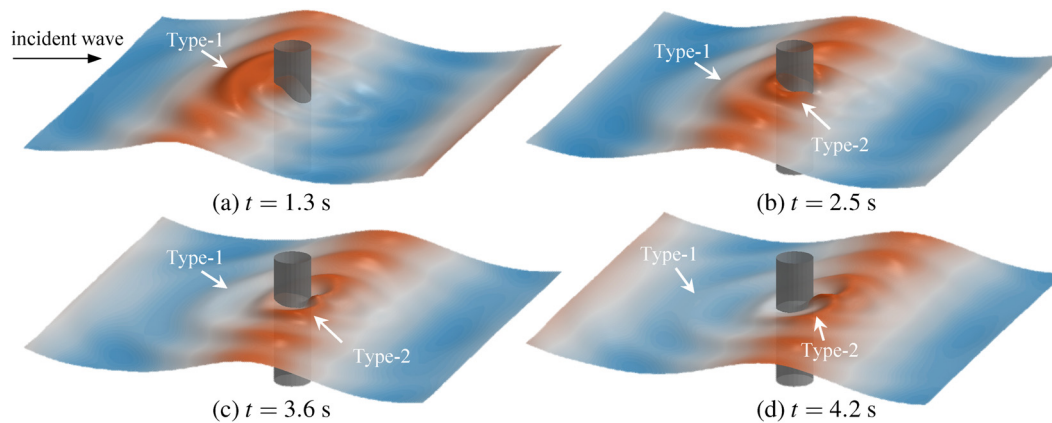**FIG. 15.** Time history of surface elevation at wave probes (T09S130).

FIG. 16. Scattered wave pattern near the cylinder at different times (T09S130). (a) $t = 1.3$, (b) $t = 2.5$, (c) $t = 3.6$, and (d) $t = 4.2$ s.
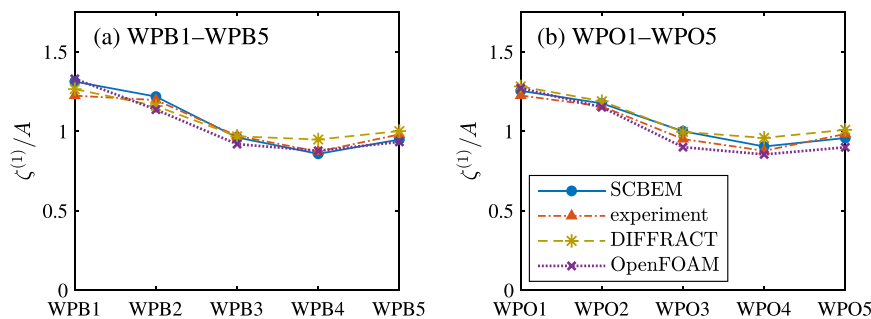

FIG. 17. First harmonic components of surface elevations at wave probes around the cylinder (T09S130). (a) Probes WPB1–WPB5 and (b) probes WPO1–WPO5.

the pre-breaking treatment, which may have caused slightly lower wave heights at WPB4 than in the experimental and CFD simulation results shown in Fig. 15(c).

The wave elevation time histories at different probes are analyzed under various conditions using FFT. The response amplitude operator (RAO) curves for the first-order harmonics of wave run-ups are plotted in Figs. 17 and 18 and compared with experimental data as well as numerical predictions by Sun *et al.* using OpenFOAM and DIFFRACT.[49] For the low steepness case (T09S130), all three numerical methods achieve satisfactory accuracy. However, for the higher steepness scenario (T09S116) where nonlinear effects are more prominent, results from DIFFRACT show some deviations from the experimental results at the probes near the wall (WPB1–WPB5). In T09S116, our PNWT still

achieves high accuracy in predicting the RAOs at the weather side probes (WPB1–WPB3), but slightly lower than the experimental data at the lee side probes (WPB4 and WPB5) due to the pre-breaking treatment in our method. Future improvements can be made by incorporating more physically realistic breaking models into the approach.

B. Diffraction of a four-cylinder array

1. Numerical setup

In this subsection, numerical simulations are conducted to replicate the benchmark experiment on four-cylinder diffraction organized by the Ocean Engineering Committee at the 27th ITTC.[48] The experiments were performed in the MARINTEK wave tank. As shown in
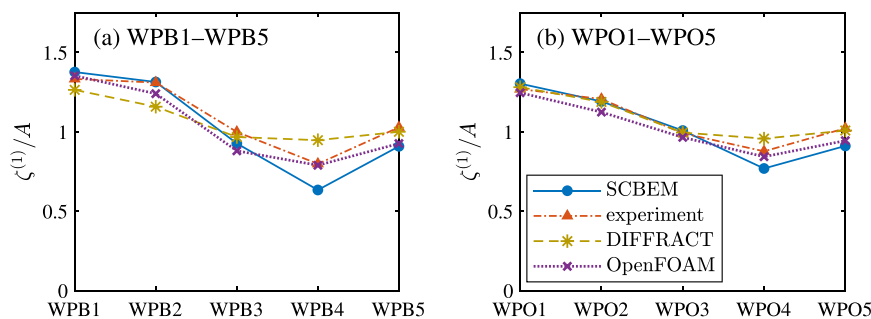

FIG. 18. First harmonic components of surface elevations at wave probes around the cylinder (T09S116). (a) Probes WPB1–WPB5 and (b) probes WPO1–WPO5.
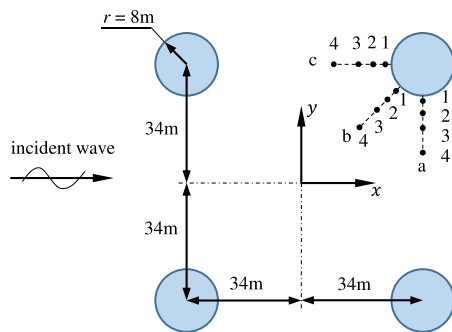
FIG. 19. Placement of four truncated cylinders (in prototype scale).

FIG. 20. Numerical discrete schematic diagram of four-cylinder diffraction simulation.

Fig. 19, the four cylinders have a radius of 8 m and a draft of 24 m, with a spacing of 34 m between their centers. Probes are arranged around the rearward cylinder along the wave direction at 90°, 135°, and 180°, denoted as a1–a4, b1–b4, and c1–c4, respectively. The distances of these probes from the center of the rearward cylinder are 8.05, 9.47, 12.75, and 16.00 m.

Regular waves with various steepness and periods are employed as incident waves. The parameters of the simulated waves for each scenario in this study are listed in Table V.

The simulations conducted in this subsection utilize the same computational domain as in Sec. III A (see Table II). Figure 20 shows the node placement near the cylinders, with local node refinement applied around each cylinder. A total of 5088 surface panels and 1144 locally refined nodes are used in the simulations. The numerical simulations are conducted with a sufficiently small time step to ensure convergence. For T09S130 scenario, simulating one wave period after reaching a steady state takes approximately 94 s.

2. Analysis of numerical results

Figure 21 presents the time histories of normalized wave elevations at probes a1–a4 after the simulations reached steady state. For an incident wave with a period of $T = 9$ s, the differences in the normalized wave height among the a-series probes under different steepness are minimal, as both exhibit similar crest and trough values. The time histories for both steepness scenarios demonstrate significant nonlinear characteristics, where the wave surface rises rapidly to reach the crest before gradually falling at a slower rate. When the steepness is $H/L = 1/16$, the higher-order wave components become more pronounced in the time history. Among the four wave probes (a1–a4), a4

TABLE V. Wave parameters for four truncated cylinders.

Name	Period T (s)	Steepness H/L	Height H (m)
T07S130	7	1/30	2.578
T07S116	7	1/16	4.969
T09S130	9	1/30	4.262
T09S116	9	1/16	8.215
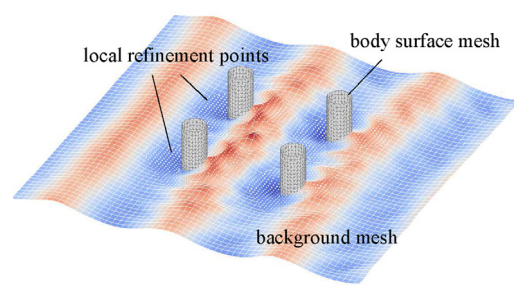
exhibits the highest wave crest, which can reach up to 1.5 times the amplitude of the incident wave.

The time histories of wave elevation are analyzed using FFT, and first harmonics (RAOs) and second harmonics (QTFs) at different wave probes are presented in Figs. 22–25. In these figures, ε_1 and ε_2 represent scenarios with small steepness ($H/L = 1/30$) and large steepness ($H/L = 1/16$), respectively. Experimental and CFD results from ITTC Ocean Engineering Committee report[48] are included for comparison. In figures, CFD-A refers to the numerical results simulated by CD-Adapco using the STAR-CCM+ software, while CFD-F refers to the numerical results simulated by Shanghai Jiao Tong University using OpenFOAM.

The RAO data in Fig. 22 indicate that our SCBEM simulation achieves prediction accuracy comparable to CFD-based NWTs. However, all numerical predictions underestimate the RAO compared to experimental results, with the RAO at probes b1 and c1 being underestimated by approximately 25% in particular. Compared to CFD predictions, our method yields slightly higher amplitudes, which may result from the potential-flow approach not accounting for viscosity effects. Among the wave probes, the weather side probes in the c-series exhibit the largest predicted RAOs, where the predicted RAO at c1 can reach 1.3, while the probes in the a-series have the smallest
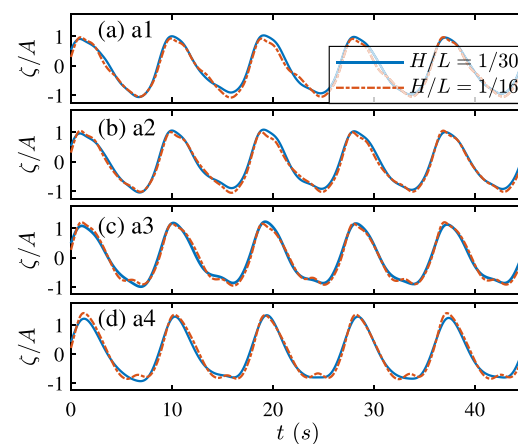

FIG. 21. Time history of probes a1–a4 after steady state for four-cylinder diffraction simulation ($T = 9$ s). Sublabels (a)–(d), respectively, represent the time history of probes a1–a4.
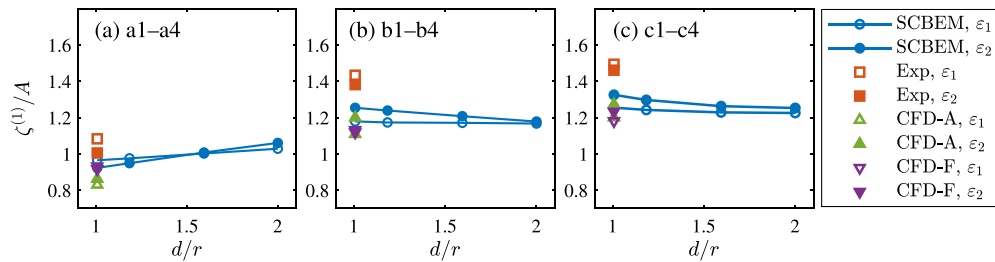
FIG. 22. First harmonic components of surface elevations for four truncated cylinders ($T = 9$ s). (a) Probes a1–a4, (b) probes b1–b4, and (c) probes c1–c4.
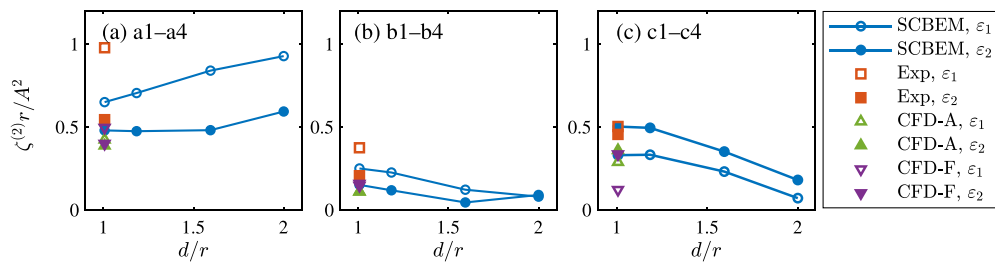

FIG. 23. Second harmonic components of surface elevations for four truncated cylinders ($T = 9$ s). (a) Probes a1–a4, (b) probes b1–b4, and (c) probes c1–c4.

FIG. 24. First harmonic components of surface elevations for four truncated cylinders ($T = 7$ s). (a) Probes a1–a4, (b) probes b1–b4, and (c) probes c1–c4.

FIG. 25. Second harmonic components of surface elevations for four truncated cylinders ($T = 7$ s). (a) Probes a1–a4, (b) probes b1–b4, and (c) probes c1–c4.
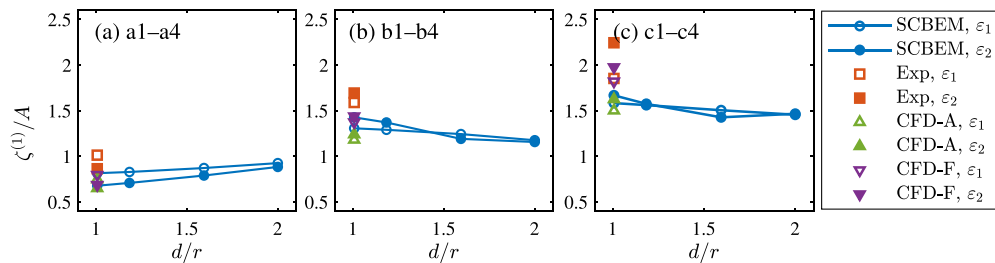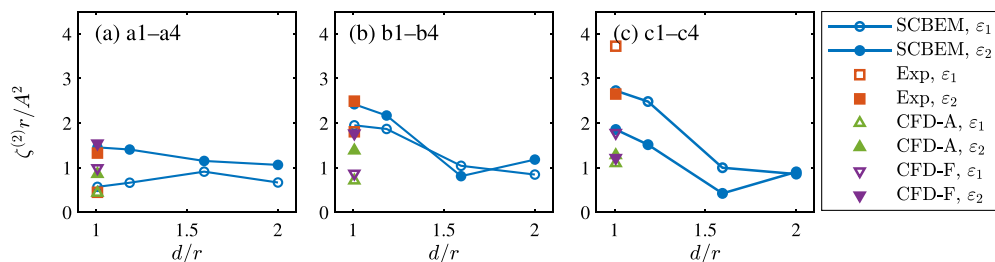
predicted RAOs, generally around 1. When the incident wave steepness is high, the nonlinearity of waves causes a slight increase in the RAOs at probes b1–b4 and c1–c4.

Figure 23 reveals significant differences in second harmonics for varying wave steepness, indicating the limitations of second-order potential-flow theory in predicting diffraction waves in a column array. The present simulations achieve prediction accuracy comparable to CFD methods when compared against experimental results. Moreover, our method generally yields higher values at probes a1, b1, and c1 than the other two CFD-based NWTs. As the distance from the cylinder increases, the QTF at probes b1–b4 and c1–c4 decreases, while the value at probes a1–a4 slightly increases.
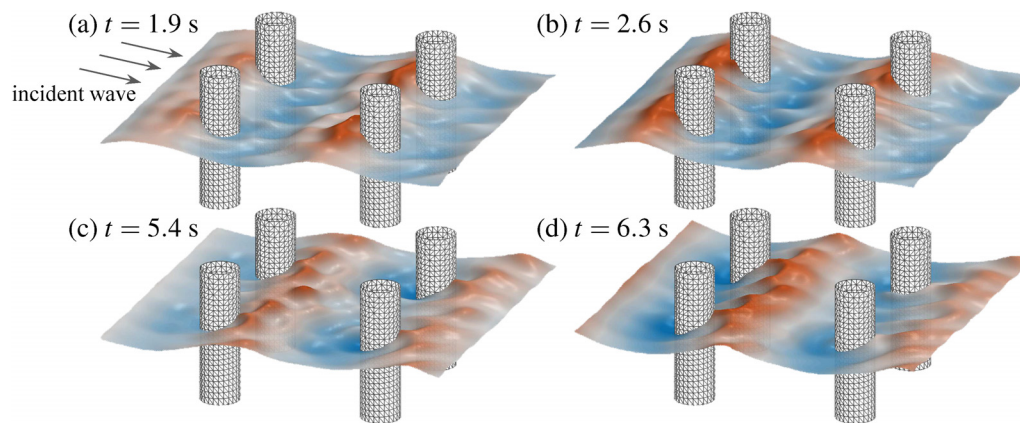
FIG. 26. Instantaneous wave pattern of four-cylinder diffraction simulation (T07S116). (a) $t = 1.9$, (b) $t = 2.6$, (c) $t = 5.4$, and (d) $t = 6.3$ s.

Figures 24 and 25, respectively, present the first and second harmonics of wave elevation for an incident wave with a period of $T = 7$ s. As the incident wavelength is nearly equal to the distance between the cylinders, the $T = 7$ s wave induces more pronounced nonlinear effects, also resulting in significantly larger harmonic components than those obtained under $T = 9$ s wave conditions. The numerical predictions of different methods for RAO and QTF trends across varying wave steepness are consistent with experimental data. Notably, in the experiment, probe c1 exhibits RAO values over two times higher than that of other probes, with our PNWT predicting an RAO of 1.7 at this location, indicating significant wave run-up.

Figure 26 presents the instantaneous wave pattern for $T = 7$ s, depicting strong interference between the cylinders and complex diffraction wave patterns. Figure 26(b) shows significant wave run-up on the weather side of the two forward cylinders after encountering the wave crest. In Fig. 26(c), there is substantial wave accumulation on the lee side of the cylinders after the wave crest passes, also with extremely steep waves appearing between the two cylinders. Figure 26(a) shows the wave pattern at probe c1 before reaching its peak wave height, exhibiting highly nonlinear waves with extreme steepness ahead of the rear cylinder. This wave may break before reaching c1 at the time depicted in Fig. 26(b), potentially explaining why the PNWT results in Fig. 24(c) are lower than those obtained using CFD-F.

C. Near-trapped modes for closely spaced columns

1. Numerical setup

When a vertical column array encounters incident waves at a certain angle and frequency, scattered waves may become *trapped* between the columns. These scattered waves are continuously reflected between the columns but cannot escape from the structure, resulting in what is known as near-trapped modes. Due to extremely low energy dissipation, scattered waves under near-trapped modes accumulate energy continuously, resulting in significant wave run-up and wave excitation forces on the columns. Chen et al.[14] and Fu et al.[15] investigated the near-trapped modes of a four-column array using the linearized potential-flow method and proposed that the use of permeable columns can reduce wave run-up and wave forces under near-trapped

modes. Gharechae further introduced the concept of Energy Transmission Index and conducted an in-depth study on the near-trapped modes of permeable barriers and circular cylinders.[16]

This section employs the proposed fully nonlinear method to simulate the case studied by Fu et al.,[15] where columns are arranged as illustrated in Fig. 27. The incident waves are obliquely angled at 45° as shown in the figure. The radius of each column is $r = 6$ m, with a spacing ratio of $r/b = 0.7$. The draft of the columns is $d = 10r$, and with respect to the incident wave conditions discussed in this section, it can be considered as deep water. In the numerical simulation, simulating one wave period after reaching a steady state takes approximately 71 s.

2. Analysis of numerical results

Regular waves with a wave steepness of $kA = 0.01$ are utilized as incident waves in numerical simulations. After the time-domain simulations reach steady state, the first harmonic components of the horizontal force on four columns are examined, producing the curve presented in Fig. 28. Here, c1–c4 denotes the columns in Fig. 27. Symmetry dictates that the horizontal force acting on column c4 is identical to that on column c2, and, therefore, not shown in the figure.
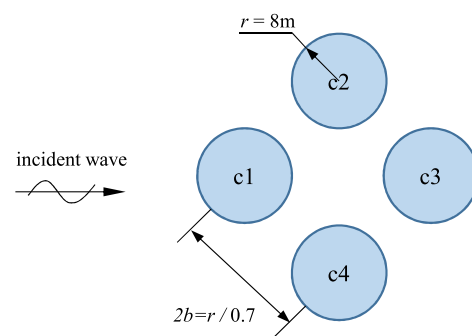

FIG. 27. Configuration for numerical simulation of near-trapped modes in a four-cylinder array.
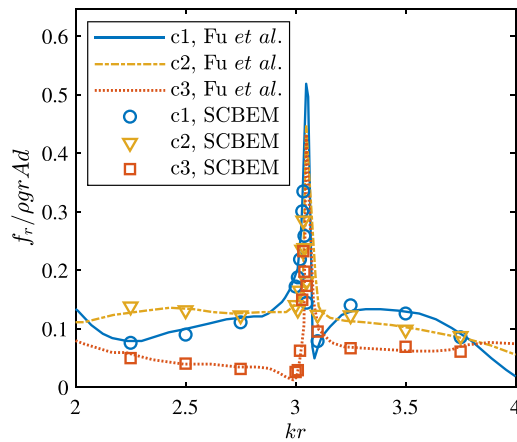
FIG. 28. Horizontal force amplitude of each column with different wavenumbers kr.

FIG. 30. Frequency components of the horizontal force on column c1 in steady state with different wavenumbers kr (incident wave steepness $kA = 0.01$).

Within the range of wavenumbers where near-trapped modes do not occur, the SCBEM predicts the same amplitude of horizontal force as the linear method of Fu et al.,[15] as shown in Fig. 28. Near the wavenumbers where near-trapped modes occur, our method successfully captures the near-trapped modes with the predicted horizontal force displaying a sudden increase concerning nearby wavenumbers. The maximum horizontal force observed through our method happened at $kr = 3.035$, with an error of less than 1% for the value of 3.048 predicted by Fu et al. based on linear theory.

Figure 29 presents the time histories of the horizontal force on column c1 for incident waves with wavenumbers $kr = 2.750$ and $kr = 3.035$. Figure 30 displays the frequency components of the horizontal force after steady state. In the case of near-trapped modes ($kr = 3.035$), the dimensionless horizontal force rapidly increases to approximately 0.15 in a short time upon encountering the incident wave and then slowly rises at an extremely low rate, taking several hundred wave periods to reach a steady state. Notably, even if the steepness of the incident wave is minimal, a significant second-order harmonic component exists in the force response depicted in Fig. 30,
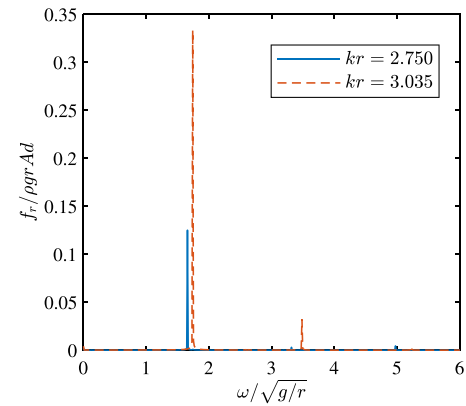
thereby imparting asymmetry to the time history of the horizontal force at $kr = 3.035$. This observation highlights the significant role of nonlinearity in near-trapped modes. For $kr = 2.750$ which do not trigger near-trapped modes, the force on the column soon reaches a steady state. The force envelope for $kr = 2.750$ exhibits fluctuations during the early stage of the time history. This phenomenon arises because the column array generates scattered wave components of the near-trapped mode frequency when excited by precursor waves. Furthermore, the energy associated with this near-trapped component requires a substantial duration to dissipate. It can be observed from Fig. 30 that the horizontal force at $kr = 2.750$ is primarily comprised of first-order harmonic, and nonlinear effects are not prominent.

Figure 31 illustrates the time-domain wave pattern of the near-trapped mode after reaching the steady state. Waves are trapped between the columns, resulting in a significant wave elevation alternation between two pairs of columns, as shown in Figs. 31(b) and 31(e). The maximum wave run-ups of the four columns are relatively consistent, with each being approximately seven times the incident wave amplitude. Columns c1 and c3 reach their maximum wave run-ups at the same moment, while columns c2 and c4 reach their maximum run-ups precisely half a wave period later.
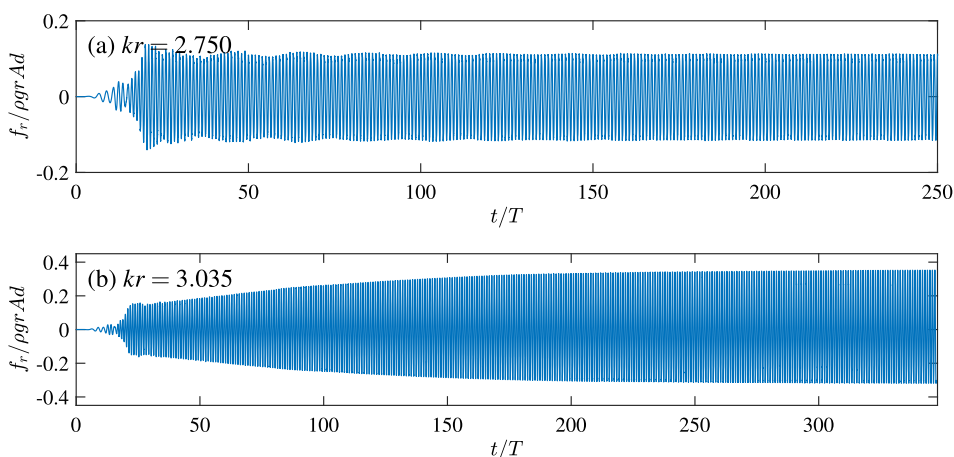

FIG. 29. Time histories of the horizontal force on column c1 under different incident waves. (a) $kr = 2.750$, $kA = 0.01$ and (b) $kr = 3.035$, $kA = 0.01$.
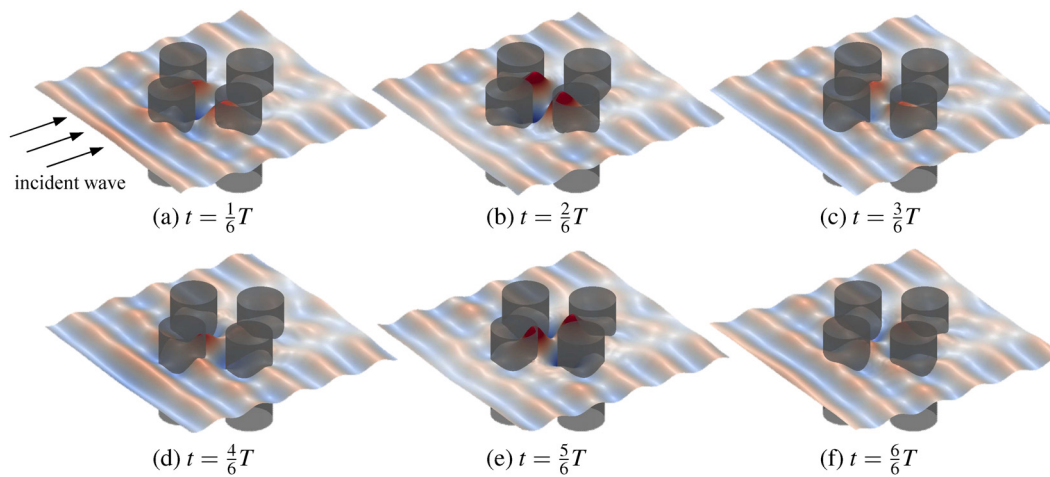
FIG. 31. Instantaneous wave pattern after steady state under an incident wave with $kr = 3.035$ and $kA = 0.01$. (a)–(f) Six different moments within one wave period T. Among them, (b) and (e) exhibit the maximum wave run-ups.

D. Narrow gap oscillations during side-by-side offloading

1. Numerical setup

In marine engineering, side-by-side offloading of oil between two FPSOs/FLNGs is a common practice, where the narrow gap between the vessels can experience significant wave resonance under incident waves, posing a risk to production safety. To explore the capability of our proposed fully nonlinear potential-flow approach, this subsection presents numerical simulations based on experiments conducted by Zhao et al.[51] In the experiments, rectangular boxes with a length of 3.33 m, a width of 0.767 m, and a draft of 0.185 m are arranged side by side with a spacing of 0.132 m, and the hull of the rectangular body has a chamfer with a radius of 0.083 m. Scaling up these dimensions, the setup can be considered as two large vessels with a length of 200 m, a width of 46 m, and a gap of 4 m side-by-side. The two floating bodies are rigidly fixed, and waves incident from the ship's side (wave angle of 90°). A probe is placed at the center of the gap to monitor the gap resonance. Figure 32 provides a discrete schematic of the numerical simulation. The PNWT is conducted using a background mesh with
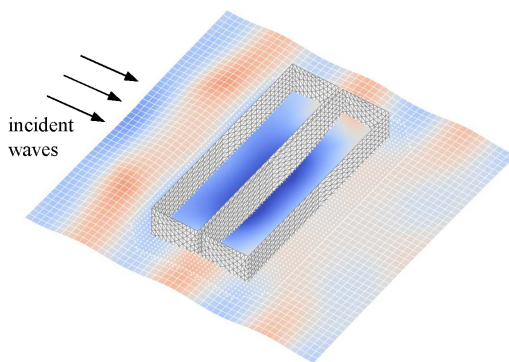
512×512 nodes, and the computational domain parameters are listed in Table VI. The grid spacing is set to 0.1 m, with a total of 4128 refined nodes near the bodies. For regular waves, the simulation time per wave period is 68.6 s.

Simulating the gap resonance RAO in the time domain presents significant technical challenges. This is not only due to the unique structure of the problem, which requires a large number of meshes, but also because the process of gradually inputting energy from incident waves into the gap until it reaches steady state is extremely time-consuming and can take tens of wave periods.[37] Conducting numerous numerical tests for regular waves to obtain RAO is clearly inefficient in this case. Hence, this section adopts an approach similar to that used in the experiments, which utilizes white noise to obtain RAO in bulk through numerical simulation. In the PNWT, two white-noise spectra with significant wave heights of $H_s = 3.8$ and 37 mm and a frequency range between 3.77 and 8.80 rad/s are generated as incident waves, and the gap response is simulated for a sufficiently long period to calculate the RAO.

2. Analysis of numerical results

Figure 33 shows a time history segment of the wave elevation measured at the center of the gap between two floating bodies for

FIG. 32. Discrete schematic of numerical simulation for gap resonance.

TABLE VI. Parameters of the computational domain for SCBEM simulation of gap resonance.

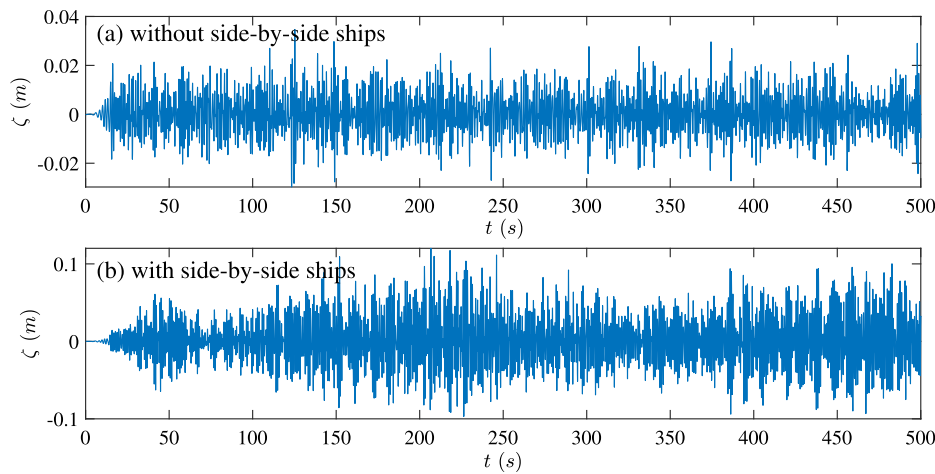| Parameter	Value
Background mesh spacing	0.1 m
Transition zone width	3 m
Size of the entire computational domain	$51.2 \times 51.2 \text{ m}^2$
Size of the BEM domain	$7.5 \times 7.5 \text{ m}^2$
Size of the inner BEM zone	$4.5 \times 4.5 \text{ m}^2$
Number of panel elements	4128
Number of refined nodes	1285
Refined node spacing	0.06 m

FIG. 33. Time history of wave elevation for numerical simulation of gap resonance ($H_s = 38$ mm). (a) Wave elevation for incident wave and (b) wave elevation for gap resonance.

$H_s = 38$ mm. Figure 33(a) is the incident wave time history at this position when there are no structures present in the computational domain, while Fig. 33(b) shows the wave elevation response induced by the same incident wave with two bodies present, although the incident wave has a small amplitude, with a maximum wave height of only about 30 mm. However, the wave elevation response in the gap exceeds 100 mm, indicating significant wave resonance and nonlinearity. This large oscillation in the gap could result in considerable changes in the instantaneous wetted surface and may exhibit strong nonlinear characteristics.

Taking the time history after $t > 100$ s, the power spectrum is drawn in Fig. 34. Figure 34(a) displays the incident wave power spectrum measured at the probe in the absence of structures, indicating good agreement between the measured wave spectrum and the target white-noise spectrum. Figure 34(b) shows the wave elevation power spectrum at the gap with two side-by-side structures present, showing four distinct resonance peaks. Dividing the response spectrum by the wave spectrum and taking the square root give the RAO of the gap resonance, as shown in Fig. 35, where the experimental and WADAM results are extracted from the study by Zhao et al.[51] The experimental RAO is obtained based on the white-noise response, and the WADAM result is computed using the linearized potential-flow theory.

The two sets of numerical experiments conducted in this study, along with the WADAM frequency domain calculation, successfully predict the gap resonance peaks, validating the accuracy of the proposed method for simulating long-term irregular waves. Nonlinear factors show little effect on the resonance amplitude, as seen in the figure where the resonance amplitude for $H_s = 3.8$ mm is similar to that for $H_s = 3.8$ mm. However, compared to the RAO at $H_s = 3.8$ mm, the gap resonance peak for $H_s = 38$ mm shifts slightly toward higher frequencies. This suggests that nonlinear factors other than viscosity may mainly increase the resonance frequency, while viscosity may play a role in controlling both the resonance frequency and amplitude. These findings are consistent with the conclusions drawn by Feng and Bai.[37]

IV. CONCLUSION

This paper presents a fully nonlinear potential-flow approach for simulating wave-body interactions that is highly efficient, suitable for large computation domains, and easy to implement. The proposed SCBEM involves splitting the hydrodynamic problem of wave–structure interaction into far-field and near-field problems, with the former efficiently modeled by a HOS solver, and the latter modeled via the BEM, resulting in significant computational cost reduction. For discretizing the BEM domain, unstructured scattering points and triangular meshes are employed, along with the RBF method facilitating information migration between time steps. To further enhance efficiency, GMRES is used for solving the source strength distribution in the
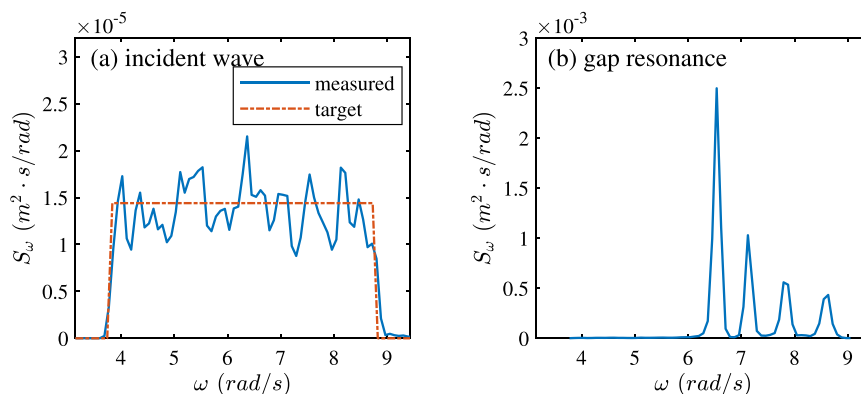

FIG. 34. Power spectrum of wave elevation for numerical simulation of gap resonance ($H_s = 38$ mm). (a) Power spectrum for incident wave and (b) power spectrum for gap resonance.
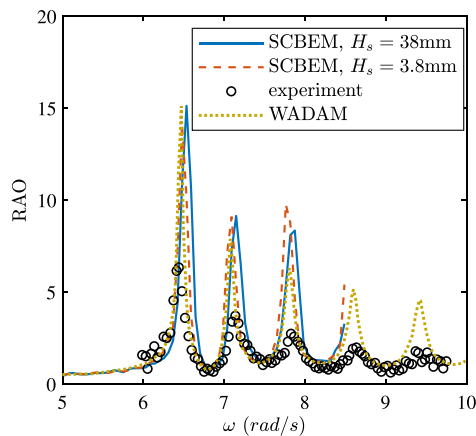
FIG. 35. RAO for wave elevation of gap resonance.

BEM domain, and the coefficient matrix product is directly computed using GPUs. By employing these methods, an efficient fully nonlinear PNWT has been developed.

To verify the accuracy of the SCBEM and evaluate its ability to simulate nonlinear problems, numerical simulations of some typical scenarios are conducted, including single-cylinder wave run-up and four-cylinder diffraction simulation. Convergence study of the single-cylinder case demonstrates that the proposed method can achieve convergence with respect to both time step and mesh resolution. Comparison with experimental and other numerical results confirms that the proposed SCBEM can accurately simulate strong nonlinear phenomena and achieve prediction accuracy comparable to CFD-based NWTs. Furthermore, white-noise numerical experiments are performed to simulate gap resonance. The numerical results show that the present PNWT can successfully perform long-term simulation of irregular waves. In various operating conditions, our PNWT exhibits high computational efficiency, requiring only 20 s per wave period for single-cylinder cases. Despite containing over 4000 surface panels and tens of thousands of free surface nodes in the BEM domain, four-cylinder and gap resonance cases can be simulated within two minutes per wave period using our PNWT, significantly faster than CFD.

Despite many promising features, the proposed method still has inherent limitations. For example, it cannot simulate wave breaking well and cannot accurately predict the amplitude of resonance peaks for gap resonance. This is mainly due to the inherent deficiency of potential-flow theory in accounting for viscosity. Since ships and marine structures often operate at high Reynolds numbers where viscosity can be neglected and other nonlinear effects may play a more important role, we believe that the proposed method can be an attractive option for researchers and engineers seeking to simulate wave-structure interactions. Moreover, the method can also provide a perspective on the flow field without viscosity, which can be used to study the role of viscosity by comparing with experimental or other viscous simulations.

ACKNOWLEDGMENTS

AUTHOR DECLARATIONS
Conflict of Interest

The authors have no conflicts to disclose.

Author Contributions

Kaiyuan Shi: Conceptualization (equal); Investigation (equal); Methodology (equal); Software (lead); Validation (equal); Visualization (lead); Writing – original draft (lead). **Renchuan Zhu:** Conceptualization (equal); Funding acquisition (lead); Investigation (equal); Methodology (equal); Supervision (lead); Validation (equal); Visualization (supporting); Writing – original draft (supporting).

DATA AVAILABILITY

The data that support the findings of this study are available from the corresponding author upon reasonable request.

REFERENCES

[1]Z. Fang, L. Xiao, H. Wei, M. Liu, and Y. Guo, "Severe wave run-ups on fixed surface-piercing square column under focused waves," Phys. Fluids **32**, 063308 (2020).

[2]Y. Ding, J. H. Walther, and Y. Shao, "Higher-order gap resonance between two identical fixed barges: A study on the effect of water depth," Phys. Fluids **34**, 052113 (2022).

[3]S. Chen, W. Zhao, and D. Wan, "On the scattering of focused wave by a finite surface-piercing circular cylinder: A numerical investigation," Phys. Fluids **34**, 035132 (2022).

[4]S. Mirjalili, S. S. Jain, and M. Dodd, "Interface-capturing methods for two-phase flows: An overview and recent developments," in *Annual Research Briefs* (Center for Turbulence Research, 2017).

[5]T. Marić, D. B. Kothe, and D. Bothe, "Unstructured un-split geometrical volume-of-fluid methods—A review," J. Comput. Phys. **420**, 109695 (2020).

[6]A. M. Miquel, A. Kamath, M. Alagan Chella, R. Archetti, and H. Bihs, "Analysis of different methods for wave generation and absorption in a CFD-based numerical wave tank," J. Mar. Sci. Eng. **6**, 73 (2018).

[7]C. Kim, A. Clement, and K. Tanizawa, "Recent research and development of numerical wave tanks—A review," Int. J. Offshore Polar Eng. **9**, 241–256 (1999).

[8]D. Fructus, D. Clamond, J. Grue, and ∅. Kristiansen, "An efficient model for three-dimensional surface wave simulations: Part I: Free space problems," J. Comput. Phys. **205**, 665–685 (2005).

[9]D. Clamond, D. Fructus, J. Grue, and ∅. Kristiansen, "An efficient model for three-dimensional surface wave simulations. Part II: Generation and absorption," J. Comput. Phys. **205**, 686–705 (2005).

[10]X. Zhang, B. Khoo, and J. Lou, "Wave propagation in a fully nonlinear numerical wave tank: A desingularized method," Ocean Eng. **33**, 2310–2331 (2006).

[11]G. Ducrozet, F. Bonnefoy, D. Le Touzé, and P. Ferrant, "A modified high-order spectral method for wavemaker modeling in a numerical wave tank," Eur. J. Mech.-B **34**, 19–34 (2012).

[12]W. Wang, A. Kamath, C. Pakozdi, and H. Bihs, "Investigation of focusing wave properties in a numerical wave tank with a fully nonlinear potential flow model," J. Mar. Sci. Eng. **7**, 375 (2019).

[13]I. Tani, "History of boundary layer theory," Annu. Rev. Fluid Mech. **9**, 87–111 (1977).

[14]J.-T. Chen, Y. Lin, Y.-T. Lee, and C. Wu, "Water wave interaction with surface-piercing porous cylinders using the null-field integral equations," Ocean Eng. **38**, 409–418 (2011).

[15]Z.-J. Fu, Z.-Y. Xie, S.-Y. Ji, C.-C. Tsai, and A.-L. Li, "Meshless generalized finite difference method for water wave interactions with multiple-bottom-seated-cylinder-array structures," Ocean Eng. **195**, 106736 (2020).

13 August 2023 00:59:22

[16] A. Gharechae and M. J. Ketabdari, "Analytical solution based on BEM to oblique waves scattering by thin arc-shaped permeable barrier applied for array of aquaculture cages," Eng. Anal. Boundary Elem. **134**, 241–258 (2022).

[17] C. Wang, S. Zheng, and Y. Zhang, "A heaving system with two separated oscillating water column units for wave energy conversion," Phys. Fluids **34**, 047103 (2022).

[18] A. Sarkar and A. Chanda, "Structural performance of a submerged bottom-mounted compound porous cylinder on the water wave interaction in the presence of a porous sea-bed," Phys. Fluids **34**, 092113 (2022).

[19] A. Chanda, A. Sarkar, and S. N. Bora, "An analytical study of scattering of water waves by a surface-piercing bottom-mounted compound porous cylinder placed on a porous sea-bed," J. Fluids Struct. **115**, 103764 (2022).

[20] A.-j. Li and Y. Liu, "Hydrodynamic performance and energy absorption of multiple spherical absorbers along a straight coast," Phys. Fluids **34**, 117102 (2022).

[21] M. S. Longuet-Higgins and E. D. Cokelet, "The deformation of steep surface waves on water—I. A numerical method of computation," Proc. R. Soc. London, A **350**, 1–26 (1976).

[22] F. Coslovich, M. Kjellberg, M. Östberg, and C.-E. Janson, "Added resistance, heave and pitch for the KVLCC2 tanker using a fully nonlinear unsteady potential flow boundary element method," Ocean Eng. **229**, 108935 (2021).

[23] S.-L. Sun, J.-L. Wang, H. Li, R.-Q. Chen, and C.-J. Zhang, "Investigation on responses and wave climbing of a ship in large waves using a fully nonlinear boundary element method," Eng. Anal. Boundary Elem. **125**, 250–263 (2021).

[24] Y. Tang, S.-L. Sun, and H.-L. Ren, "Numerical investigation on a container ship navigating in irregular waves by a fully nonlinear time domain method," Ocean Eng. **223**, 108705 (2021).

[25] M. Irannezhad, A. Eslamdoost, M. Kjellberg, and R. E. Bensow, "Investigation of ship responses in regular head waves through a fully nonlinear potential flow approach," Ocean Eng. **246**, 110410 (2022).

[26] K. Nabors, F. Korsmeyer, F. T. Leighton, and J. White, "Preconditioned, adaptive, multipole-accelerated iterative methods for three-dimensional first-kind integral equations of potential theory," SIAM J. Sci. Comput. **15**, 713–735 (1994).

[27] Y.-L. Shao and O. M. Faltinsen, "Towards efficient fully-nonlinear potential-flow solvers in marine hydrodynamics," in *International Conference on Offshore Mechanics and Arctic Engineering* (American Society of Mechanical Engineers, 2012), Vol. 44915, pp. 369–380.

[28] J. C. Harris, E. Dombre, M. Benoit, S. T. Grilli, and K. I. Kuznetsov, "Nonlinear time-domain wave-structure interaction: A parallel fast integral equation approach," Int. J. Numer. Methods Fluids **94**, 188–222 (2022).

[29] J. R. Phillips and J. K. White, "A precorrected-FFT method for electrostatic analysis of complicated 3-D structures," IEEE Trans. Comput.-Aided Des. Integr. Circuits Syst. **16**, 1059–1072 (1997).

[30] H. Yan and Y. Liu, "An efficient high-order boundary element method for nonlinear wave–wave and wave-body interactions," J. Comput. Phys. **230**, 402–424 (2011).

[31] W. Li, W. Chen, and Z. Fu, "Precorrected-FFT accelerated singular boundary method for large-scale three-dimensional potential problems," Commun. Comput. Phys. **22**, 460–472 (2017).

[32] P. C. De Haas and P. J. Zandbergen, "The application of domain decomposition to time-domain computations of nonlinear water waves with a panel method," J. Comput. Phys. **129**, 332–344 (1996).

[33] W. Bai and R. Eatock Taylor, "Numerical simulation of fully nonlinear regular and focused wave diffraction around a vertical cylinder using domain decomposition," Appl. Ocean Res. **29**, 55–71 (2007).

[34] T. Geng, H. Liu, and F. Dias, "Solitary-wave loads on a three-dimensional submerged horizontal plate: Numerical computations and comparison with experiments," Phys. Fluids **33**, 037129 (2021).

[35] A. P. Engsig-Karup, M. G. Madsen, and S. L. Glimberg, "A massively parallel GPU-accelerated model for analysis of fully nonlinear free surface waves," Int. J. Numer. Methods Fluids **70**, 20–36 (2012).

[36] Y.-L. Shao and O. M. Faltinsen, "A harmonic polynomial cell (HPC) method for 3D Laplace equation with application in marine hydrodynamics," J. Comput. Phys. **274**, 312–332 (2014).

[37] X. Feng and W. Bai, "Wave resonances in a narrow gap between two barges using fully nonlinear numerical simulation," Appl. Ocean Res. **50**, 119–129 (2015).

[38] V. E. Zakharov, "Stability of periodic waves of finite amplitude on the surface of a deep fluid," J. Appl. Mech. Tech. Phys. **9**, 190–194 (1972).

[39] J. Romate, "Absorbing boundary conditions for free surface waves," J. Comput. Phys. **99**, 135–145 (1992).

[40] J. D. Fenton, "A fifth-order stokes theory for steady waves," J. Waterw., Port, Coastal, Ocean Eng. **111**, 216–234 (1985).

[41] K. Shi, R. Zhu, and D. Xu, "A spectral coupling layer technique for the simulation of nonlinear surface gravity waves," Ocean Eng. (unpublished).

[42] D. G. Dommermuth and D. K. P. Yue, "A high-order spectral method for the study of nonlinear gravity waves," J. Fluid Mech. **184**, 267–288 (1987).

[43] B. J. West, K. A. Brueckner, R. S. Janda, D. M. Milder, and R. L. Milton, "A new numerical method for surface hydrodynamics," J. Geophys. Res. **92**, 11803, https://doi.org/10.1029/JC092iC11p11803 (1987).

[44] X. Zhang, P. Bandyk, and R. F. Beck, "Seakeeping computations using double-body basis flows," Appl. Ocean Res. **32**, 471–482 (2010).

[45] J. L. Hess and A. O. Smith, "Calculation of potential flow about arbitrary bodies," Prog. Aerosp. Sci. **8**, 1–138 (1967).

[46] J. Lyness and D. Jespersen, "Moderate degree symmetric quadrature rules for the triangle," IMA J. Appl. Math. **15**, 19–32 (1975).

[47] P. Atkinson and S. McIntosh-Smith, "On the performance of parallel tasking runtimes for an irregular fast multipole method application," in *Scaling OpenMP for Exascale Performance and Portability: 13th International Workshop on OpenMP (IWOMP 2017), Stony Brook, NY, 20–22 September 2017* (Springer, 2017), pp. 92–106.

[48] Ocean Engineering Committee, "Final report and recommendations to the 27th ITTC," in *Proceedings of the 27th International Towing Tank Conference* (2014), Vol. 3, pp. 263–331.

[49] L. Sun, J. Zang, L. Chen, R. E. Taylor, and P. Taylor, "Regular waves onto a truncated circular column: A comparison of experiments and simulations," Appl. Ocean Res. **59**, 650–662 (2016).

[50] C. Swan and R. Sheikh, "The interaction between steep waves and a surface-piercing column," Philos. Trans. R. Soc., A **373**, 20140114 (2015).

[51] W. Zhao, Z. Pan, F. Lin, B. Li, P. H. Taylor, and M. Efthymiou, "Estimation of gap resonance relevant to side-by-side offloading," Ocean Eng. **153**, 1–9 (2018).

13 August 2023 00:59:22